

The method of the approximate inverse for atmospheric tomography

Daniel Gerth Bernadette N. Hahn Ronny Ramlau

DK-Report No. 2014-12

12 2014

A-4040 LINZ, ALTENBERGERSTRASSE 69, AUSTRIA

Supported by

Austrian Science Fund (FWF)

Upper Austria

Editorial Board: Bruno Buchberger
Bert Jüttler
Ulrich Langer
Manuel Kauers
Esther Klann
Peter Paule
Clemens Pechstein
Veronika Pillwein
Silviu Radu
Ronny Ramlau
Josef Schicho
Wolfgang Schreiner
Franz Winkler
Walter Zulehner

Managing Editor: Silviu Radu

Communicated by: Ulrich Langer
Walter Zulehner

DK sponsors:

- **Johannes Kepler University Linz (JKU)**
- **Austrian Science Fund (FWF)**
- **Upper Austria**

The method of the approximate inverse for atmospheric tomography

Daniel Gerth, Bernadette N. Hahn and Ronny Ramlau

November 20, 2014

Abstract

In this paper, we propose a new approach for the atmospheric tomography based on the method of the approximate inverse. The image quality of earth-bound telescopes is severely degraded by turbulences of the atmosphere of the earth. In order to receive sharp images, the incoming light is corrected for these distortions using deformable mirrors. In atmospheric tomography, the turbulence profile is reconstructed so that the shape of the mirror can be adjusted in an optimal way. We perform this reconstruction step by applying the method of the approximate inverse to Multi-Conjugate Adaptive Optics. We show that the approximate inverse leads to efficient algorithms and give numerical examples.

1 Introduction

The planned next generation of telescopes, e.g. the European Extremely Large Telescope (E-ELT) or the Thirty Meter Telescope (TMT), depend on Adaptive Optics (AO) technology in order to achieve highest image quality. The image quality of ground based telescopes is heavily affected by turbulences in the atmosphere. In Adaptive Optics, measurements of incoming wavefronts from bright guide stars are used to determine the shape of deformable mirrors (DM) in such a way that, after reflection of the incoming light on the deformable mirror, the influence of the turbulent atmosphere is removed from the astronomical images. In order to compute the optimal

mirror shapes of the DMs from the wavefront sensor measurements, an *Inverse Problem* has to be solved. As the atmosphere changes rapidly, the shapes of the DMs have to be computed between 500-3000 times per second (depending on the AO system). Thus, powerful reconstruction methods are needed in order to solve the related Inverse Problem in the available time. For a survey on Inverse Problems in Adaptive Optics we refer to [15].

The simplest AO system, which is already used at existing telescopes, is Single Conjugate Adaptive Optics (SCAO). SCAO only uses one (natural) guide star, i.e., a bright star outside the atmosphere, one wavefront sensor and one deformable mirror. As the natural guide star is far away, the incoming wavefronts are assumed to be plane. However, this property is destroyed once the light passes through the atmosphere. Wavefront sensor data are used to reconstruct the shape of the wavefront, and based on the reconstruction the DM is deformed such that the outgoing wavefront is “flattened” (see Figure 1) - the image of the guide star, and consequently all astronomical objects close to the guide star, are sharp again. In the SCAO case, the Inverse Problem

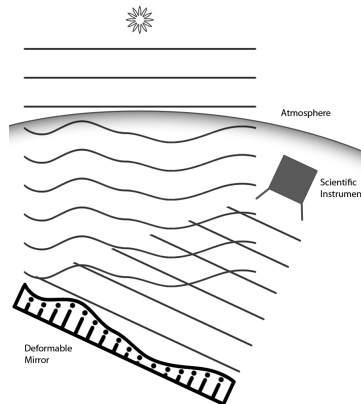


Figure 1: Principle of SCAO

that has to be solved simply consist in the reconstruction of the incoming wavefronts from wavefront sensor measurements, see, e.g., [16, 17, 2, 18, 19, 20, 21]. Second generation AO systems as Multi Conjugate Adaptive Optics (MCAO) and Multi Object Adaptive Optics (MOAO) use several guide stars and wavefront sensors as well as multiple deformable mirrors, conjugated to different heights, in order to obtain a high imaging quality over a large field of view or to image multiple astronomical images at the same time.

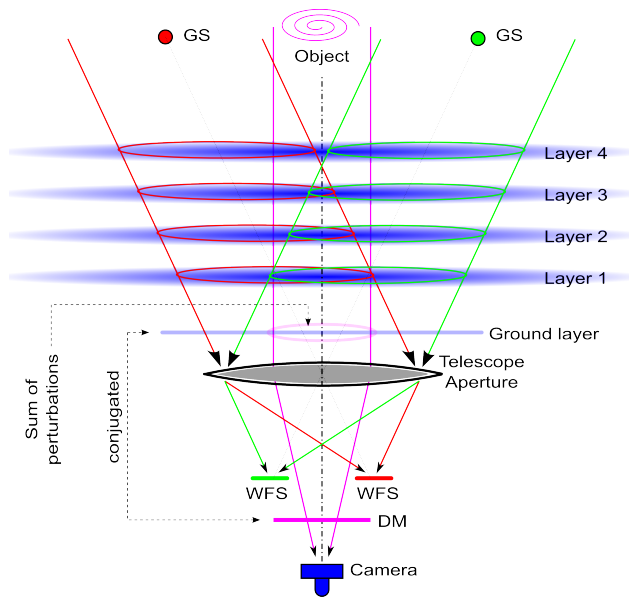


Figure 2: Principle of MCAO, courtesy of [1]

This paper is concerned with a new inversion approach for MCAO. The setup of an MCAO system is, e.g., described in [15, 22]. MCAO systems are based on a reconstruction of the turbulence of the atmosphere above the telescope. To this end, the wavefronts of the incoming light from several well separated guide stars is measured by wavefront sensors. The connection between the incoming wavefronts and the turbulence is described by the *atmospheric tomography operator*, see Section 2. Inverting the atmospheric tomography operator thus gives a reconstruction of the turbulence profile of the atmosphere. Atmospheric tomography for telescopes is a variant of limited angle tomography, which is known to be a severely ill-posed problem, see, e.g., [3, 23]. However, a common assumption in atmospheric tomography is that turbulences in the atmosphere are restricted to certain heights. As a consequence, only atmospheric layers are reconstructed, see Figure 2.

As mentioned above, MCAO uses several deformable mirrors for the correction. The mirrors are conjugated to different heights and are deformed based on the reconstructed turbulence profile, see Figure 3. In the simplest case an MCAO system has as many DMs as layers. In this case, a single DM is used for correcting the influence of a single layer. In reality, however, one

usually has more layers than deformable mirrors (e.g., the MCAO system at the E-ELT will use 3 DMs). Therefore, the shape of the mirrors has to be determined by an additional optimization routine, cf. [24, 25].

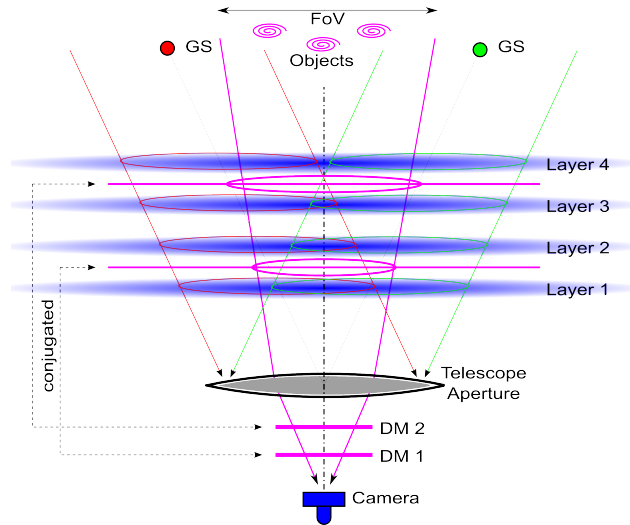


Figure 3: Mirrors in an MCAO system, courtesy of [1]

Several reconstruction approaches have been developed for MCAO. A standard approach is to consider the operator \mathbf{R} that maps the wavefront sensor data to the commands that drive the deformable mirror. The inversion process then involves either the inversion of large matrices [26] or the solution of large linear systems, which can be achieved, e.g., by CG methods [5, 6, 7, 27] or preconditioned CG methods [28, 29, 30, 2, 31]. Also, Fourier transform based reconstructors have been proposed [32, 33, 23].

In order to further speed up the computations, iterative methods using a specific representation of the covariance matrix of the statistics of the turbulence matrix have been investigated, e.g., the Fractal Iterative Method (*FrIM*) [34] and a wavelet based method (*FEWHA*), [35, 36]. Finally, a class of methods has been developed that solve the subproblems for MCAO (wavefront reconstruction, atmospheric tomography and mirror fitting) sequentially. From the so called *three step methods* we would like to mention in particular the Kaczmarz method [25, 37, 38, 39].

In this paper, we present a new reconstruction method for atmospheric

tomography, to determine the turbulence profile of the atmosphere from incoming wavefronts from guide stars. Therefore, our reconstructor can be used as an ingredient for a three step method. The proposed method is based on the method of the *approximate inverse*, which was first introduced in [10] and analyzed in [8]. The main idea of the method is to precompute a problem dependent *reconstruction kernel*. The reconstruction from measured data is then obtained by forming inner products between the data and the reconstruction kernel. Using properties of the described operator, this method leads to very efficient algorithms as required in MCAO.

The paper is organized as follows: In Section 2 we explain the principle of MCAO in more details and present its mathematical formulation. Section 3 is concerned with the method of the approximate inverse, first introduced for scalar functions and then extended to the case of vector-valued functions. We apply the method of the approximate inverse to our specific problem in Section 4 and describe the reconstruction algorithm. Numerical aspects are discussed and the reconstruction quality is evaluated in Section 5.

2 Principle of Multi Conjugate Adaptive Optics

A key factor in AO systems are the guide stars. In this paper, we consider two types of guide stars that are used to measure the incoming wavefronts. Natural guide stars (NGS) are simply real, bright stars. The wavefront of such a natural guide star can be assumed to be planar before entering the atmosphere since it travels an enormous distance in space. However, as such a guide star has to fulfil several physical and technical conditions, the coverage of the sky with suitable natural guide stars is rather low, and artificial guide stars have to be used. These are created by projecting a laser beam to the sky, hence they are called laser guide stars (LGS). At an altitude of about 90 km, there is a layer of sodium with a thickness of about 10 km. The sodium atoms are excited by the laser beam and the returning light can be used to measure the wavefront.

The price to pay for this type of guide stars are additional effects that reduce the quality of reconstruction. In our simple model, laser guide stars are modelled as a point at altitude 90 km. Hence the propagation of the light from this point to the telescope pupil has the form of a cone rather than a

cylinder, as would be the case for natural guide stars; see Figure 2. This is called the cone-effect; it will be included in our model. Other effects not considered here are tip-tilt indetermination [37, 39] and spot elongation [39].

The idea of MCAO, see Figure 3; is to use the information of several (natural and/or laser) guide stars to compute the shape of several deformable mirrors which are situated at ground level, but conjugated to a certain altitude of the atmosphere. That way, the combination of all deformable mirrors can be seen as an approximation to the turbulence profile of the atmosphere.

The atmosphere itself is modelled as a vector of two dimensional functions rather than one 3D object. Each of these functions is called a layer of the atmosphere. Hence, for MCAO, we aim at the reconstruction of a finite number L of turbulent layers $\Phi^{(l)}$, located at heights h_l , $l = 1, \dots, L$, each corresponding to a deformable mirror conjugated to height h_l . Available measurements are the incoming wavefronts φ_{α_g} , $g = 1, \dots, G$, of the guide stars which we identify by their angle, or more precisely by the corresponding unit vector, α_g . Because of the cone effect we define $\mu_{l,\alpha_g} := \frac{H_g - h_l}{H_g}$ for laser guide stars. In this notation, we allow a different scaling not only for each layer l , but also in each direction α_g . The case of a natural guide star is covered by setting $\mu_{l,\alpha_g} := 1$.

At altitude h_l , we can only hope to reconstruct what is “seen” by the sensors, i.e. the layer $\Phi^{(l)}$ will only be reconstructed within the area

$$\Omega_l = \bigcup_{g=1}^G \Omega_D^{\mu_{l,\alpha_g}}(h_l \alpha_g),$$

where

$$\Omega_D^{\mu_{l,\alpha_g}}(h_l \alpha_g) := \{\rho \in \mathbb{R}^2 : \mu_{l,\alpha_g}^{-1}(\rho - h_l \alpha_g) \in \Omega_D\}$$

and Ω_D represents the telescope with radius D , i.e.,

$$\Omega_D = \{r \in \mathbb{R}^2 : \|r\| \leq D\}.$$

We consider $\Phi^{(l)} \in L_2(\Omega_l)$ and collect all the layers in a vector

$$\Phi := (\Phi^{(1)}, \dots, \Phi^{(L)})^T \in \bigotimes_{l=1}^L L_2(\Omega_l).$$

On this space, an inner product is defined via

$$\langle \Phi, \Psi \rangle_{\bigotimes_{l=1}^L L_2(\Omega_l)} := \sum_{l=1}^L \frac{1}{c_l} \langle \Phi^{(l)}, \Psi^{(l)} \rangle_{L_2(\Omega_l)}, \quad (1)$$

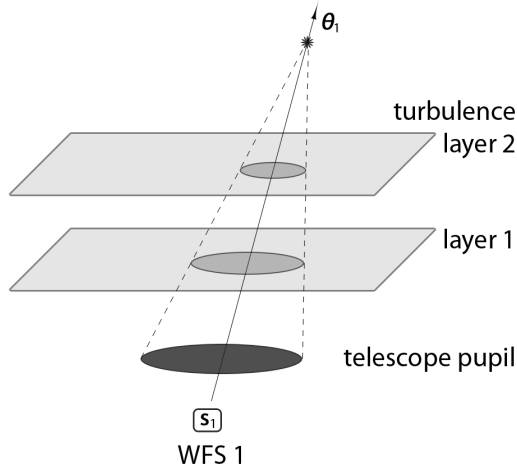


Figure 4: Due to the laser being focused in a single point, the wavefronts travel in a cone-shaped domain

where c_l is the (known) relative strength of a layer in the atmosphere. The operator describing atmospheric tomography is given by

$$A : \bigotimes_{l=1}^L L_2(\Omega_l) \longrightarrow (L_2(\Omega_D))^G, \\ A\Phi(r) := \left(\sum_{l=1}^L \Phi^{(l)}(\mu_{l,\alpha_g} r + h_l \alpha_g) \right)_{g=1,\dots,G}, \quad r \in \Omega_D. \quad (2)$$

Hence, the goal is the reconstruction of Φ from the measured data

$$A\Phi = \varphi,$$

where

$$\varphi = (\varphi_{\alpha_1}, \dots, \varphi_{\alpha_G})^T.$$

3 Method of the Approximate Inverse

3.1 Reconstruction of scalar functions

The method of the approximate inverse is a regularization scheme to solve an ill-posed inverse problem

$$Af = g \quad (3)$$

with measured data g and an operator A between Hilbert spaces [8, 10] or Banach spaces [11, 12]. In the following, we introduce the idea of this method in the case of a linear bounded operator $A : L_2(\Omega_X) \rightarrow L_2(\Omega_Y)$ with bounded subsets $\Omega_X \subset \mathbb{R}^n$ and $\Omega_Y \subset \mathbb{R}^m$. In this setting, $f \in L_2(\Omega_X)$ and $g \in L_2(\Omega_Y)$ are scalar valued functions. In the subsequent section, the method is then extended to vector-valued functions as occur in atmospheric tomography.

In order to get a stable approximation of the function f from the ill-posed problem (3), we consider a smoothed version

$$f^\gamma(x) := \langle f, e_x^\gamma \rangle_{L_2(\Omega_X)} \quad (4)$$

with a prescribed mollifier $e_x^\gamma \in L_2(\Omega_X)$, $\gamma > 0$. The calculation of linear functionals leads to regularization methods, see the theoretical result of Likht [9] and the algorithmic of Louis and Maaß [10]. The mollifier e_x^γ can be seen as an approximation to the delta distribution δ_x . A precise definition of a mollifier is given in the following, see [13].

Definition 3.1. For all $x \in \Omega_X$, $\gamma > 0$ let $e_x^\gamma \in L_2(\Omega_X)$ with

$$\int_{\Omega_X} e_x^\gamma(z) dz = 1.$$

Let further

$$f^\gamma(x) = \int_{\Omega_X} f(z) e_x^\gamma(z) dz$$

converge to f in $L_2(\Omega_X)$ as $\gamma \rightarrow 0$. Then e_x^γ is called a mollifier.

Now, instead of the original equation (3), one solves the auxiliary problem

$$A^* \psi_x^\gamma = e_x^\gamma \quad (5)$$

where A^* denotes the adjoint of A . Thus, the mollified version f^γ can be computed from the measured data as a functional with ψ_x^γ ,

$$f^\gamma(x) = \langle f, e_x^\gamma \rangle_{L_2(\Omega_X)} = \langle f, A^* \psi_x^\gamma \rangle_{L_2(\Omega_X)} = \langle Af, \psi_x^\gamma \rangle_{L_2(\Omega_Y)} = \langle g, \psi_x^\gamma \rangle_{L_2(\Omega_Y)}.$$

The auxiliary problem (5) is only solvable if $e_x^\gamma \in \mathcal{R}(A^*)$. If at least $e_x^\gamma \in \mathcal{D}((A^*)^\dagger)$ with $(A^*)^\dagger$ denoting the pseudo inverse of A^* , the function ψ_x^γ can be computed by minimizing the defect $\|A^* \psi_x^\gamma - e_x^\gamma\|^2$, which is equivalent to the solution of the normal equation

$$AA^* \psi_x^\gamma = Ae_x^\gamma. \quad (6)$$

We will show in Section 4.2 that in our application $e_x^\gamma \notin \mathcal{R}(A^*)$, i.e., we will only be able to reconstruct approximate reconstruction kernels by solving the normal equation (6). Hence, throughout the paper we will focus on the theory for this case. Although now

$$f^\gamma(x) = \langle f, e_x^\gamma \rangle_{L_2(\Omega_X)} \approx \langle f, A^* \psi_x^\gamma \rangle_{L_2(\Omega_X)} = \langle Af, \psi_x^\gamma \rangle_{L_2(\Omega_Y)} = \langle g, \psi_x^\gamma \rangle_{L_2(\Omega_Y)}$$

holds only approximately, we will write the equality sign for the sake of convenience.

Definition 3.2. *Let e_x^γ be a mollifier. The operator $S^\gamma : L_2(\Omega_Y) \rightarrow L_2(\Omega_X)$ with*

$$S^\gamma g(x) := \langle g, \psi_x^\gamma \rangle_{L_2(\Omega_Y)},$$

where ψ_x^γ solves either (5) or (6), is called the approximate inverse of A to compute an approximation of f . The function ψ_x^γ is called reconstruction kernel.

The regularization property of the approximate inverse S^γ is verified in [8].

Since the auxiliary problem is independent of the data, the reconstruction kernels ψ_x^γ can be precomputed. However, the dependence on the reconstruction point $x \in \Omega_X$ requires the solution of a possibly different auxiliary problem for each of these points. Using suitable invariances of the operator A , this computational effort can be dramatically reduced, see e.g. [8, 13].

Theorem 3.3. *Let $T_1^x : L_2(\Omega_X) \rightarrow L_2(\Omega_X)$, $T_2^x : L_2(\Omega_Y) \rightarrow L_2(\Omega_Y)$ and $T_3^x : L_2(\Omega_Y) \rightarrow L_2(\Omega_Y)$ be linear, bounded operators for $x \in \Omega_X$ satisfying*

$$AT_1^x = T_2^x A, \quad T_2^x AA^* = AA^* T_3^x. \quad (7)$$

Further assume that the mollifier e_x^γ is generated by T_1^x , i.e. $e_x^\gamma := T_1^x e^\gamma$ with $e^\gamma \in \mathcal{D}((A^*)^\dagger)$. If ψ^γ solves $AA^* \psi^\gamma = Ae^\gamma$, then the special reconstruction kernels ψ_x^γ are given by

$$\psi_x^\gamma = T_3^x \psi^\gamma.$$

Proof Using the intertwining properties (7), it holds

$$Ae_x^\gamma = AT_1^x e^\gamma = T_2^x Ae^\gamma = T_2^x AA^* \psi^\gamma = AA^* T_3^x \psi^\gamma = AA^* \psi_x^\gamma.$$

□

According to the proof, it is sufficient if the invariance property $AT_1^x = T_2^x A$ holds for the specific prescribed mollifier e^γ .

Using such invariances, only one single auxiliary problem has to be solved, and the special reconstruction kernels ψ_x^γ are generated by this solution ψ^γ and the operator T_3^x , leading to the reconstruction

$$f^\gamma(x) = \langle g, T_3^x \psi^\gamma \rangle_{L_2(\Omega_Y)}. \quad (8)$$

3.2 Reconstruction of vector-valued functions

In the previous section, the regularization scheme was presented in the case of scalar-valued functions. However, the mathematical model of atmospheric tomography is described by an operator relating vector-valued functions, namely $\Phi \in \bigotimes_{l=1}^L L_2(\Omega_l)$, which comprises the layers of the atmosphere, and the available data $\varphi \in (L_2(\Omega_D))^G$, see (2). The method of the approximate inverse has been extended to the reconstruction of vector fields already in the case of the three-dimensional Doppler transform [14]. In the following, we apply the method to the setting presented in Section 2 by choosing appropriate mollifiers for the different layers.

Let δ_x denote the delta distribution with $x \in \mathbb{R}^2$. The first layer of the atmosphere, i.e. the first component of the vector $\Phi = (\Phi^{(1)}, \dots, \Phi^{(L)})^T$, is given by

$$\begin{aligned} \Phi^{(1)}(x) &= \langle \Phi^{(1)}, \delta_x \rangle_{L_2(\Omega_1)} \\ &= \left(\frac{1}{c_1} \langle \Phi^{(1)}, c_1 \delta_x \rangle_{L_2(\Omega_1)} + \sum_{l=2}^L \frac{1}{c_l} \langle \Phi^{(l)}, 0 \rangle_{L_2(\Omega_l)} \right) \\ &= \langle \Phi, \bar{\delta}_{x,1} \rangle_{\bigotimes_{l=1}^L L_2(\Omega_l)} \end{aligned}$$

Here $\bar{\delta}_{x,1} := (c_1 \delta_x, 0, \dots, 0)^T$ denotes an L -dimensional vector, where the first component is $c_1 \delta_x$ and the remaining components correspond to the zero functions in $L_2(\Omega_l)$, $l = 2, \dots, L$. Replacing the delta-distribution δ_x by a scalar-valued mollifier $e_x^\gamma \in L_2(\Omega_1)$ leads to the mollified version

$$\Phi_\gamma^{(1)}(x) := \langle \Phi, \bar{e}_{x,1}^\gamma \rangle_{\bigotimes_{l=1}^L L_2(\Omega_l)}$$

with $\bar{e}_{x,1}^\gamma := (c_1 e_x^\gamma, 0, \dots, 0)^T \in \bigotimes_{l=1}^L L_2(\Omega_l)$. Analogously, we obtain a mollified version $\Phi_\gamma^{(l)}$ of the l -th layer by

$$\Phi_\gamma^{(l)}(x) = \langle \Phi, \bar{e}_{x,l}^\gamma \rangle_{\bigotimes_{i=1}^L L_2(\Omega_i)} \quad \text{for } x \in \Omega_l \quad (9)$$

where

$$\bar{e}_{x,l}^\gamma := (c_l e_x^\gamma \delta_{i,l})_{i=1,\dots,L} \quad (10)$$

with the Kronecker symbol $\delta_{i,l}$. This notation abbreviates the fact that only the l -th component of $\bar{e}_{x,l}^\gamma$ is nonzero with a scalar-valued mollifier $e_x^\gamma \in L_2(\Omega_l)$. Especially, it can be easily verified that $\bar{e}_{x,l}^\gamma$ is in fact a mollifier to approximate $\Phi^{(l)}$ in accordance to Definition 3.1.

Now, let $\Psi_l^\gamma \in L_2(\Omega_D)^G$ solve the normal equation

$$AA^*\Psi_l^\gamma = A\bar{e}_l^\gamma, \quad (11)$$

where $\bar{e}_l^\gamma := \bar{e}_{0,l}^\gamma \in \mathcal{D}((A^*)^\dagger)$ is, without loss of generality, the mollifier centred at zero and let $T_1^x : \bigotimes_{l=1}^L L_2(\Omega_l) \rightarrow \bigotimes_{l=1}^L L_2(\Omega_l)$, $T_2^x : (L_2(\Omega_D))^G \rightarrow (L_2(\Omega_D))^G$ and $T_3^x : (L_2(\Omega_D))^G \rightarrow (L_2(\Omega_D))^G$ denote suitable invariance operators for A . Then, the mollified version of the layer $\Phi^{(l)}$ can be computed from the measured data via

$$\Phi_\gamma^{(l)}(x) = \langle \varphi, T_3^x \Psi_l^\gamma \rangle_{(L_2(\Omega_D))^G} = \sum_{g=1}^G \langle \varphi_{\alpha_g}, (T_3^x \Psi_l^\gamma)_g \rangle_{L_2(\Omega_D)}.$$

4 Application to Atmospheric Tomography

This section deals with the derivation of suitable invariance operators in order to obtain efficient algorithms and with the calculation of the reconstruction kernel.

For each layer $\Phi^{(l)}$, the operator A only takes the respective set Ω_l into account. Thus, an intertwining property (7) holds only for reconstruction points $x \in \bigcap_{g=1}^G \Omega_D^{\mu_l, \alpha_g}(h_l \alpha_g)$, i.e. only on the part of the layer which is seen from all angles α_g , $g = 1, \dots, G$. To overcome this restriction, a continuation of A to the whole spatial domain \mathbb{R}^2 is presented in the following. For this new operator, an intertwining property can be found which holds for all reconstruction points $x \in \Omega_l$. Hence, the method of the approximate inverse applied to this operator leads to an efficient reconstruction of the whole layer. Despite the slightly changed setting, the searched-for layers will still be adequately reconstructed, as discussed in Section 4.3.

4.1 Continuation of the operator A

Each layer $\Phi^{(l)} \in L_2(\Omega_l)$ can be extended to \mathbb{R}^2 via

$$\tilde{\Phi}^{(l)}(\rho) := \begin{cases} \Phi^{(l)}, & \rho \in \Omega_l \\ 0, & \rho \notin \Omega_l \end{cases}. \quad (12)$$

We now consider the mapping

$$\begin{aligned} \mathcal{A} : (L_2(\mathbb{R}^2))^L &\longrightarrow (L_2(\mathbb{R}^2))^G \\ \mathcal{A}\tilde{\Phi}(r) &:= \left(\sum_{l=1}^L \tilde{\Phi}^{(l)}(\mu_{l,\alpha_g}r + h_l\alpha_g) \right)_{g=1,\dots,G}. \end{aligned} \quad (13)$$

This new operator considers the whole spatial domain \mathbb{R}^2 instead of only the subsets Ω_l , $l = 1, \dots, L$. With the correlation of $\tilde{\Phi}$ and Φ and $r \in \Omega_D$, it is for $g \in \{1, \dots, G\}$

$$\begin{aligned} \left(\mathcal{A}\tilde{\Phi} \right)_g(r) &= \sum_{l=1}^L \tilde{\Phi}^{(l)}(\mu_{l,\alpha_g}r + \alpha_g h_l) \\ &= \sum_{l=1}^L \Phi^{(l)}(\mu_{l,\alpha_g}r + \alpha_g h_l) = (A\Phi)_g(r) = \varphi_{\alpha_g}(r). \end{aligned}$$

Hence, on the telescope, $\mathcal{A}\tilde{\Phi}$ corresponds to the measured data. However, the extended operator \mathcal{A} leads to artificial data for $r \notin \Omega_D$. Denote

$$\tilde{\Omega} := \bigcup_{g=1}^G \{r \in \mathbb{R}^2 \setminus \Omega_D : \exists l \text{ with } \mu_{l,\alpha_g}r + \alpha_g h_l \in \Omega_l\}. \quad (14)$$

This set $\tilde{\Omega}$ comprises all points r outside the telescope which are still so close that $\mu_{l,\alpha_g}r + \alpha_g h_l \in \Omega_l$ for at least one height h_l and one unit vector α_g . For $r \in \mathbb{R}^2 \setminus (\tilde{\Omega} \cup \Omega_D)$, it holds

$$\mathcal{A}\tilde{\Phi}^{(l)}(r) = 0,$$

and for $r \in \tilde{\Omega}$, it is

$$\mathcal{A}\tilde{\Phi}^{(l)}(r) = \tilde{\varphi}(r)$$

with an unknown function $\tilde{\varphi} \neq 0$. However, the effect of this deviation on the reconstruction of $\Phi^{(l)}$ is very weak, as discussed in Section 4.3.

Analogously to (1), the inner product on $\bigotimes_{l=1}^L L_2(\mathbb{R}^2)$ is given by

$$\langle \Phi, \Psi \rangle_{\bigotimes_{l=1}^L L_2(\mathbb{R}^2)} := \sum_{l=1}^L \frac{1}{c_l} \langle \Phi^{(l)}, \Psi^{(l)} \rangle_{L_2(\mathbb{R}^2)}.$$

In order to apply the method of the approximate inverse, we first have to compute the adjoint \mathcal{A}^* of \mathcal{A} .

Theorem 4.1. *The adjoint of \mathcal{A} is given by*

$$\begin{aligned} \mathcal{A}^* : (L_2(\mathbb{R}^2))^G &\longrightarrow \bigotimes_{l=1}^L L_2(\mathbb{R}^2) \\ (\mathcal{A}^* \varphi)^{(l)}(\rho) &= c_l \sum_{g=1}^G \mu_{l,\alpha_g}^{-2} \varphi_{\alpha_g} \left(\mu_{l,\alpha_g}^{-1} (\rho - \alpha_g h_l) \right), \quad l = 1, \dots, L. \end{aligned} \quad (15)$$

Proof Using the definition of \mathcal{A} , we obtain

$$\begin{aligned} \langle \mathcal{A}\Phi, \varphi \rangle_{(L_2(\mathbb{R}^2))^G} &= \sum_{g=1}^G \langle (\mathcal{A}\Phi)_g, \varphi_{\alpha_g} \rangle_{L_2(\mathbb{R}^2)} \\ &= \sum_{g=1}^G \int_{\mathbb{R}^2} \sum_{l=1}^L \Phi^{(l)}(\mu_{l,\alpha_g} r + h_l \alpha_g) \varphi_{\alpha_g}(r) \, dr. \end{aligned}$$

With the substitution $\rho := \mu_{l,\alpha_g} r + h_l \alpha_g$, it holds

$$\begin{aligned} \langle \mathcal{A}\Phi, \varphi \rangle_{(L_2(\mathbb{R}^2))^G} &= \sum_{g=1}^G \sum_{l=1}^L \int_{\mathbb{R}^2} \mu_{l,\alpha_g}^{-2} \Phi^{(l)}(\rho) \varphi_{\alpha_g}(\mu_{l,\alpha_g}^{-1} (\rho - h_l \alpha_g)) \, d\rho \\ &= \sum_{l=1}^L \int_{\mathbb{R}^2} \Phi^{(l)}(\rho) \sum_{g=1}^G \mu_{l,\alpha_g}^{-2} \varphi_{\alpha_g}(\mu_{l,\alpha_g}^{-1} (\rho - h_l \alpha_g)) \, d\rho \\ &= \sum_{l=1}^L \frac{1}{c_l} \left\langle \Phi^{(l)}, c_l \sum_{g=1}^G \mu_{l,\alpha_g}^{-2} \varphi_{\alpha_g}(\mu_{l,\alpha_g}^{-1} (\cdot - h_l \alpha_g)) \right\rangle_{L_2(\mathbb{R}^2)} \\ &= \langle \Phi, \mathcal{A}^* \varphi \rangle_{\bigotimes_{l=1}^L L_2(\mathbb{R}^2)}. \end{aligned}$$

□

In order to solve the normal equation (11) and define proper intertwining operators, we will use the following result on the interaction of \mathcal{A} and \mathcal{A}^* .

Theorem 4.2. *It holds*

$$\mathcal{A}\mathcal{A}^* = B + \lambda I$$

with the identity operator I , $\lambda := (\lambda_g)_{g=1,\dots,G}$ where $\lambda_g := \sum_{l=1}^L c_l \mu_{l,\alpha_g}^{-2}$ and $B\Psi := (B_g\Psi)_{g=1,\dots,G}$,

$$B_g\Psi(r) := \sum_{l=1}^L c_l \sum_{i=1, i \neq g}^G \mu_{l,\alpha_i}^{-2} \Psi_i \left(\frac{\mu_{l,\alpha_g} r + \mu_{l,\alpha_i}^{-1} h_l (\alpha_g - \alpha_i)}{\mu_{l,\alpha_i}} \right). \quad (16)$$

Proof Due to the definition of the operators \mathcal{A} (13) and \mathcal{A}^* (15), we obtain for $g = 1, \dots, G$

$$\begin{aligned}
(\mathcal{A}\mathcal{A}^*\Psi)_g(r) &= \sum_{l=1}^L (\mathcal{A}^*\Psi)^{(l)}(\mu_{l,\alpha_g}r + h_l\alpha_g) \\
&= \sum_{l=1}^L c_l \sum_{i=1}^G \mu_{l,\alpha_i}^{-2} \Psi_i(\mu_{l,\alpha_i}^{-1}((\mu_{l,\alpha_g}r + h_l\alpha_g) - h_l\alpha_i)) \\
&= \sum_{l=1}^L c_l \left(\sum_{i=1, i \neq g}^G \mu_{l,\alpha_i}^{-2} \Psi_i\left(\frac{\mu_{l,\alpha_g}}{\mu_{l,\alpha_i}}r + \mu_{l,\alpha_i}^{-1}h_l(\alpha_g - \alpha_i)\right) + \mu_{l,\alpha_g}^{-2} \Psi_g(r) \right) \\
&= \sum_{l=1}^L c_l \sum_{i=1, i \neq g}^G \mu_{l,\alpha_i}^{-2} \Psi_i\left(\frac{\mu_{l,\alpha_g}}{\mu_{l,\alpha_i}}r + \mu_{l,\alpha_i}^{-1}h_l(\alpha_g - \alpha_i)\right) + \sum_{l=1}^L c_l \mu_{l,\alpha_g}^{-2} \Psi_g(r) \\
&= B_g \Psi(r) + \lambda_g \Psi_g
\end{aligned}$$

with B and λ defined above. \square

Using this representation, we obtain the following invariances.

Theorem 4.3. *Let $\bar{e}_l^\gamma(\rho) = (c_l e^\gamma \delta_{i,l})$ be the mollifier from (10) centred at zero, with $l \in \{1, \dots, L\}$ arbitrary but fixed. Define for $j = 1, \dots, L$ the linear operator*

$$\begin{aligned}
T_{1,l}^x : \bigotimes_{j=1}^L L_2(\mathbb{R}^2) &\longrightarrow \bigotimes_{j=1}^L L_2(\mathbb{R}^2), \quad (T_{1,l}^x \bar{e}_l^\gamma)^{(j)}(\rho) = (\bar{e}_l^\gamma)^{(j)} \delta_{j,l} \quad \text{and} \\
T_{2,l}^x : (L_2(\mathbb{R}^2))^G &\longrightarrow (L_2(\mathbb{R}^2))^G, \quad (T_{2,l}^x \Psi)_g(r) := \Psi_g\left(r - \frac{x}{\mu_{l,\alpha_g}}\right)
\end{aligned}$$

for $g = 1, \dots, G$. If $\mu_{l,\alpha_g} = \mu_{l,\alpha_i}$, $i, g \in \{1, \dots, G\}$, for all $l = 1, \dots, L$, then it holds

$$\mathcal{A}T_{1,l}^x \bar{e}_l^\gamma = T_{2,l}^x \mathcal{A} \bar{e}_l^\gamma, \quad T_{2,l}^x \mathcal{A}\mathcal{A}^* = \mathcal{A}\mathcal{A}^* T_{2,l}^x. \quad (17)$$

Proof Using the definition of the operators T_1^x and $T_{2,l}^x$, we obtain for $g = 1, \dots, G$

$$\begin{aligned}
(\mathcal{A}T_1^x \bar{e}_l^\gamma)_g(r) &= \sum_{j=1}^L (T_1^x \bar{e}_l^\gamma)^{(j)}(\mu_{j,\alpha_g}r + h_j\alpha_g) \\
&= c_l e^\gamma (\mu_{l,\alpha_g}r + h_l\alpha_g - x) \\
&= c_l e^\gamma \left(\mu_{l,\alpha_g} \left(r - \frac{x}{\mu_{l,\alpha_g}} \right) + h_l\alpha_g \right) \\
&= \sum_{j=1}^L (\bar{e}_l^\gamma)^{(j)} \left(\mu_{j,\alpha_g} \left(r - \frac{x}{\mu_{l,\alpha_g}} \right) + h_j\alpha_g \right) \\
&= (\mathcal{A} \bar{e}_l^\gamma)_g \left(r - \frac{x}{\mu_{l,\alpha_g}} \right) \\
&= (T_{2,l}^x \mathcal{A} \bar{e}_l^\gamma)_g(r).
\end{aligned}$$

For the second invariance, we have the following situation, see Theorem 4.2 for the representation of \mathcal{AA}^* ,

$$\begin{aligned}
& (T_{2,l}^x \mathcal{AA}^* \Psi)_g(r) = (\mathcal{AA}^* \Psi)_g \left(r - \frac{x}{\mu_{l,\alpha_g}} \right) \\
& = \sum_{j=1}^L c_l \sum_{i=1, i \neq g}^G \mu_{j,\alpha_i}^{-2} \Psi_i \left(\frac{\mu_{j,\alpha_g}}{\mu_{j,\alpha_i}} \left(r - \frac{x}{\mu_{l,\alpha_g}} \right) + \mu_{j,\alpha_i}^{-1} h_j(\alpha_g - \alpha_i) \right) \\
& \quad + \lambda_g \Psi_g \left(r - \frac{x}{\mu_{l,\alpha_g}} \right). \tag{18}
\end{aligned}$$

On the other hand, we obtain

$$\begin{aligned}
& (\mathcal{AA}^* T_{2,l}^x \Psi)_g(r) \\
& = \sum_{j=1}^L c_l \sum_{i=1, i \neq g}^G \mu_{j,\alpha_i}^{-2} \Psi_i \left(\frac{\mu_{j,\alpha_g}}{\mu_{j,\alpha_i}} \left(r - \frac{\mu_{j,\alpha_i} x}{\mu_{j,\alpha_g} \mu_{l,\alpha_i}} \right) + \mu_{j,\alpha_i}^{-1} h_j(\alpha_g - \alpha_i) \right) \\
& \quad + \lambda_g \Psi_g \left(r - \frac{x}{\mu_{l,\alpha_g}} \right). \tag{19}
\end{aligned}$$

Hence, with $\mu_{j,\alpha_i} = \mu_{j,\alpha_g}$ and $\mu_{l,\alpha_i} = \mu_{l,\alpha_g}$, it is $T_{2,\ell}^x \mathcal{AA}^* = \mathcal{AA}^* T_{2,\ell}^x$. \square

Theorem 4.3 reveals an issue when laser guide stars and natural guide stars are combined. Comparing the action of $T_{2,l}^x$ in (18) and (19), respectively, one can spot a difference in the ‘‘cross-projections’’, i.e., when projecting a component Ψ_i on a layer and then projecting it back down in direction α_g , $i \neq g$. The difference lies in the scaling factor of the shift, $r - \frac{x}{\mu_{l,\alpha_g}}$ compared to $r - \frac{\mu_{j,\alpha_i} x}{\mu_{j,\alpha_g} \mu_{l,\alpha_i}}$. In case we only consider either natural guide stars or laser guide stars, it is $\mu_{j,\alpha_i} = \mu_{j,\alpha_g}$ for all i, g , hence the invariance holds true. If both types of guide stars are mixed, however, this factor adds a systematic error in the invariances. Hence, we cannot expect the approximate inverse to perform as well for mixed guide stars as for a single type of guide stars. This problem may to some extent be avoided when tip/tilt indetermination of laser guide stars is part of the model. In this case, the natural guide stars can be used only to correct the reconstructions of the layers performed with laser guide stars. This so called separate tip/tilt reconstruction technique is described in [37].

4.2 Calculation of the reconstruction kernel

To compute the reconstruction kernels, we have to solve the auxiliary problem

$$\mathcal{A}^* \Psi_{x,l}^\gamma = \bar{e}_{x,l}^\gamma \tag{20}$$

for each point x we wish to reconstruct. The following Lemma shows that it is not possible to find an exact solution.

Lemma 4.4. *Let $\bar{e}_{x,l}^\gamma$ as in (9). Then $\bar{e}_{x,l}^\gamma \notin \mathcal{R}(\mathcal{A}^*)$.*

Proof Assume $\bar{e}_{x,l}^\gamma \in \mathcal{R}(\mathcal{A}^*)$. Hence $\bar{e}_{x,l}^\gamma \in \overline{\mathcal{R}(\mathcal{A}^*)} = \mathcal{N}(\mathcal{A})^\perp$, i.e., $\langle \bar{e}_{x,l}^\gamma, \Phi \rangle_{\otimes_{l=1}^L L_2(\mathbb{R}^2)} = 0$ for all $\Phi \in \mathcal{N}(\mathcal{A})$. Let $\tilde{\Phi}$ constant on each layer, $\tilde{\Phi} := (C_l \chi_{\Omega_l})_{l=1,\dots,L}$ with $C_l \in \mathbb{R}$, $\sum_{l=1}^L C_l = 0$. Then $\mathcal{A}\tilde{\Phi} = 0$, i.e., $\tilde{\Phi} \in \mathcal{N}(\mathcal{A})$ but

$$\langle \bar{e}_{x,l}^\gamma, \tilde{\Phi} \rangle_{\otimes_{l=1}^L L_2(\mathbb{R}^2)} = \langle e_x^\gamma, \tilde{\Phi}^{(l)} \rangle_{L_2(\Omega_l)} = C_l \langle e_x^\gamma, 1 \rangle_{L_2(\Omega_l)} \neq 0$$

because of Definition 3.1. Hence $\bar{e}_{x,l}^\gamma \notin \mathcal{N}(\mathcal{A})^\perp = \overline{\mathcal{R}(\mathcal{A}^*)}$, contradicting the original assumption. \square

Since $\bar{e}_{x,l}^\gamma \notin \mathcal{R}(\mathcal{A}^*)$, we solve the normal equation

$$\mathcal{A}\mathcal{A}^*\Psi_{x,l}^\gamma = \mathcal{A}\bar{e}_{x,l}^\gamma \quad (21)$$

instead of (20). In order to circumvent the dependency of this equation on the point x , we use the invariance properties (17) of \mathcal{A} and $\mathcal{A}\mathcal{A}^*$. Hence the mollifiers $\bar{e}_{x,l}^\gamma$ are generated by

$$\bar{e}_{x,l}^\gamma = T_{1,l}^x \bar{e}_l^\gamma \quad (22)$$

with $\bar{e}_l^\gamma := (c_l e^\gamma \delta_{i,l})_{i=1\dots L}$ analogously to (10). Again, $e^\gamma \in L_2(\mathbb{R}^2)$ is a prescribed mollifier and $\delta_{i,l}$ represents the Kronecker symbol. According to Theorem 3.3 and Theorem 4.3, the corresponding special reconstruction kernels $\Psi_{x,l}^\gamma$ are given by

$$(\Psi_{x,l}^\gamma)_g(r) = (T_{2,l}^x \Psi_l^\gamma)_g(r) = (\Psi_l^\gamma)_g\left(r - \frac{x}{\mu_{l,\alpha_g}}\right),$$

where Ψ_l^γ solves

$$\mathcal{A}\mathcal{A}^*\Psi_l^\gamma = \mathcal{A}\bar{e}_l^\gamma \quad (23)$$

i.e., Ψ_l^γ minimizes $\|\mathcal{A}\Psi - \bar{e}_l^\gamma\|^2$. It remains to solve this problem once for each layer $l = 1, \dots, L$.

A common method for solving equations of type (23) are iterative methods, in particular gradient methods. Starting from an initial guess, one iterates

$$\Psi_l^\gamma \leftarrow \Psi_l^\gamma - \tau(\mathcal{A}\mathcal{A}^*\Psi_l^\gamma - \mathcal{A}\bar{e}_l^\gamma) \quad (24)$$

until a stopping criterion is met, e.g., a maximum number of iterations. The steplength τ is used to ensure and speed up convergence and has to be chosen appropriately. With $\mathcal{A}\mathcal{A}^* = B + \lambda I$ from Theorem 4.2, (24) can be written

$$\Psi_l^\gamma \leftarrow (1 - \tau\lambda)\Psi_l^\gamma - \tau(B\Psi_l^\gamma - \mathcal{A}\bar{e}_l^\gamma).$$

This procedure updates all G components of Ψ_l^γ at once. However, the numerical results obtained with this approach were of low quality. Alternatively, one may update each component separately and immediately use the updated information in the next step. This approach was introduced by Kaczmarz for the solution of linear systems of equations. It can be extended to more general settings, in particular to adaptive optics, see, e.g., [39, 25]. In each step, we now minimize $\|\mathcal{A}\Psi_l^\gamma - \bar{e}_l^\gamma\|^2$ in direction of component $(\Psi_l^\gamma)_g$ in a cyclical way. The gradient w.r.t. to the g -th component is given by

$$\nabla_g \|\mathcal{A}\Psi_l^\gamma - \bar{e}_l^\gamma\|^2 = (\mathcal{A}\mathcal{A}^*\Psi_l^\gamma - \mathcal{A}\bar{e}_l^\gamma)_g = \lambda_g(\Psi_l^\gamma)_g + B_g\Psi_l^\gamma - (\mathcal{A}\bar{e}_l^\gamma)_g$$

With this as descent direction we construct an iterative Kaczmarz-type algorithm. Let $\bar{k} := \text{mod}(k, G) + 1$. Then, again starting from an initial guess which in practice we simply chose zero, we update

$$(\Psi_l^\gamma)_{\bar{k}} \leftarrow (1 - \tau_k \lambda_{\bar{k}})(\Psi_l^\gamma)_{\bar{k}} - \tau_k (B_{\bar{k}}\Psi_l^\gamma - (\mathcal{A}\bar{e}_l^\gamma)_{\bar{k}}) \quad (25)$$

for $k = 1, 2, \dots$ until a stopping criterion is met. In our numerical experiments we let

$$\tau_k = \frac{\|\lambda_{\bar{k}}(\Psi_l^\gamma)_{\bar{k}} + B_{\bar{k}}\Psi_l^\gamma - (\mathcal{A}\bar{e}_l^\gamma)_{\bar{k}}\|_{(L^2(\mathbb{R}^2))}}{\|\mathcal{A}^*(\lambda_{\bar{k}}(\Psi_l^\gamma)_{\bar{k}} + B_{\bar{k}}\Psi_l^\gamma - (\mathcal{A}\bar{e}_l^\gamma)_{\bar{k}})\|_{\otimes_{l=1}^L L_2(\mathbb{R}^2)}}. \quad (26)$$

This choice of τ_k minimizes the residual in the search direction, c.f. [4],

$$\tau_k = \min_{\tau} \|\mathcal{A}^*(\Psi_l^\gamma + \tau(\lambda_{\bar{k}}(\Psi_l^\gamma)_{\bar{k}} + B_{\bar{k}}\Psi_l^\gamma - (\mathcal{A}\bar{e}_l^\gamma)_{\bar{k}})) - \bar{e}_l^\gamma\|_{\otimes_{l=1}^L L_2(\mathbb{R}^2)}^2.$$

With the calculated Ψ_l^γ we can then reconstruct the layer l in any point $x \in \Omega_l$ via

$$\Phi_\gamma^{(l)}(x) = \langle \mathcal{A}\Phi, T_{2,l}^x \Psi_l^\gamma \rangle_{(L_2(\mathbb{R}^2))^G}. \quad (27)$$

Remark 4.5. We shortly want to discuss another set of invariance operators which will reduce the computational cost of the reconstruction of the layers

significantly. However, these alternative operators can only be defined when either only natural guide stars or only laser guide stars are used. Let \bar{e}_l^γ be again the mollifier from (10) centered at zero, with $l \in \{1, \dots, L\}$ arbitrary but fixed. Let $\mu_{l,\alpha_g} = \mu_{l,\alpha_i}$ for $g, i \in \{1, \dots, G\}$ for all $l = 1, \dots, L$, and define $\mu_l := \mu_{l,\alpha_g}$. Define for $j = 1, \dots, L$ the linear operator

$$T_{1,\mu_l}^x : \bigotimes_{j=1}^L L_2(\mathbb{R}^2)^L \longrightarrow \bigotimes_{j=1}^L L_2(\mathbb{R}^2)^L, \quad (T_{1,l}^x \bar{e}_l^\gamma)^{(j)}(\rho) = (\bar{e}_l^\gamma)^{(j)} \delta_{j,l}, \quad \text{and} \\ T_2^x : L_2(\mathbb{R}^2)^G \longrightarrow L_2(\mathbb{R}^2)^G, \quad (T_2^x \Psi)_g(r) := \Psi_g(r - x)$$

for $g = 1, \dots, G$. Then it holds

$$\mathcal{A}T_{1,\mu_l}^x \bar{e}_l^\gamma = T_2^x \mathcal{A} \bar{e}_l^\gamma, \quad T_2^x \mathcal{A} \mathcal{A}^* = \mathcal{A} \mathcal{A}^* T_2^x.$$

Thus, it is

$$\bar{e}_{x,l}^\gamma(\rho) = T_{1,\mu_l}^x \bar{e}_l^\gamma(\rho) = (c_l e^\gamma(\rho_l - \mu_l x) \delta_{i,l})_{i=1\dots L},$$

leading to

$$\langle \Phi, \bar{e}_{x,l}^\gamma \rangle_{\bigotimes_{i=1}^L L_2(\mathbb{R}^2)} = \langle \Phi^{(l)}, e_l^\gamma(\cdot - \mu_l x) \rangle_{L_2(\mathbb{R}^2)} = \Phi_\gamma^{(l)}(\mu_l x).$$

Hence, the mollified version $\langle \Phi, \bar{e}_{x,l}^\gamma \rangle_{\bigotimes_{i=1}^L L_2(\mathbb{R}^2)}$ approximates a scaled version of the layer $\Phi^{(l)}$, instead of the layer itself.

The corresponding reconstruction kernels represent then unscaled translated versions of Ψ_l^γ ,

$$\Psi_{x,l}^\gamma(r) = T_2^x \Psi_l^\gamma(r) = \Psi_l^\gamma(r - x).$$

Thus, the functional $\langle \varphi, \Psi_{x,l}^\gamma \rangle_{L_2(\mathbb{R}^2)^G}$ can be computed without interpolation of the data vector. Instead, this interpolation step is transferred to an interpolation on the layer. For a discussion on the numerical effort we refer to Section 5.3.

4.3 The extension error

Our main goal is the reconstruction of the layers $\Phi^{(l)}$, $l = 1 \dots L$, from the measured data $A\Phi = \varphi$. Using the extension $\tilde{\Phi}$ of Φ to the whole spatial domain \mathbb{R}^2 , (12), there is the following relation between $\mathcal{A}\tilde{\Phi}$ and $A\Phi$. Since

$$\mathcal{A}\tilde{\Phi}(r) = \begin{cases} A\Phi(r) & r \in \Omega_D \\ 0 & r \in \mathbb{R}^2 \setminus (\Omega_D \cup \tilde{\Omega}) \\ \tilde{\varphi}(r) & r \in \tilde{\Omega} \end{cases}$$

with an unknown function $\tilde{\varphi} \neq 0$ and $\tilde{\Omega}$ defined in (14). Now, for $x \in \Omega_l$, it is

$$\begin{aligned}\Phi_\gamma^{(l)}(x) &= \tilde{\Phi}_\gamma^{(l)}(x) = \langle \mathcal{A}\tilde{\Phi}, T_{2,l}^x \Psi_l^\gamma \rangle_{(L_2(\mathbb{R}^2))^G} \\ &= \langle A\Phi, T_{2,l}^x \Psi_l^\gamma \rangle_{(L_2(\Omega_D))^G} + \langle \tilde{\varphi}, T_{2,l}^x \Psi_l^\gamma \rangle_{L_2(\tilde{\Omega})} \\ &= c_l \langle A\Phi, T_{2,\mu_l}^x \Psi_l^\gamma \rangle_{(L_2(\Omega_D))^G} + \epsilon.\end{aligned}$$

The angles α_g cover just a small range, so the domain $\tilde{\Omega}$ will be relatively small compared to Ω_D . Besides, with the distance of r to Ω_D getting larger, less layers give a contribution to $\sum_{l=1}^L \Phi^{(l)}(\mu_l r + h_l \alpha_g)$, i.e. the value of $\tilde{\varphi}(r)$ is getting smaller. Altogether, the error ϵ will be small, so we approximate

$$\Phi_\gamma^{(l)}(x) = \langle A\Phi, T_{2,\mu_l}^x \Psi_l^\gamma \rangle_{(L_2(\Omega_D))^G}. \quad (28)$$

5 Numerical Results

Several tests are performed to show the quality of the approximate inverse for atmospheric tomography. The computations are performed with our simulation tool. In our basic setup we consider a telescope with 42m mirror diameter, as originally proposed for the E-ELT. The guide stars are positioned in a circle of 3.75 arcmins for laser guidestars and 5 arcmin for natural guide stars, respectively, each equipped with a Shack-Hartmann wavefront sensor with 84×84 subapertures and a field of view of 10 arcmin. Note that, due to the systematic error that occurs when both guide star types are used, we only consider either natural guide stars or laser guide stars. The error on the measurements of the wavefront sensor is assumed to be low due to a high number of photons per subaperture. The atmosphere is simulated with 9 layers, moving at a speed of roughly 15 m/s with a Fried parameter $r_0 = 20$ cm in K-band. The outer scale for the van Karman turbulence model is 20m. Three deformable mirrors are simulated, conjugated to heights of 0m, 4000m and 12700m. Hence, we seek to reconstruct an artificial atmosphere consisting of 3 layers at heights $h_1 = 0$ m, $h_2 = 4000$ m and $h_3 = 12700$ m. The relative strength of the layers are $c_1 = 0.6$, $c_2 = 0.2$ and $c_3 = 0.2$, respectively. The incoming wavefronts φ_{α_g} , $g = 1, \dots, G$ are reconstructed from the wavefront sensors with CuReD [21].

5.1 Reconstruction Method

The reconstruction of each layer $\Phi^{(l)}$ requires three basic steps. First, the vectors \bar{e}_l^γ and hence the mollifier $e^\gamma \in L_2(\mathbb{R}^2)$ has to be set up. Since we are free to choose the parameter γ , we might make a different choice for each layer l . Hence, γ_l denotes the mollification parameter used to reconstruct layer l . In our first simulations we chose the Gaussian

$$e^{\gamma_l}(\rho) := \frac{1}{2\pi\gamma_l^2} \exp\left(-\frac{\|\rho\|^2}{2\gamma_l^2}\right)$$

with $\gamma_l > 0$. For this mollifier, it holds $\|e^{\gamma_l}\|_{L_2(\mathbb{R}^2)} = 1$. However, since we reconstruct directly on the actuators of the deformable mirrors, our discretization is fixed. Due to it being rather coarse, it was not possible to find an appropriate value of γ . Instead, we followed the idea that the mollifier is supposed to approximate the delta distribution. Therefore, let Δ_l be the spacing of the actuators of the mirror conjugated to height h_l . Then we let

$$e^{\gamma_l}(\rho) = \begin{cases} \gamma_l \Delta_l^{-2}, & \rho = 0 \\ 0, & \rho \neq 0 \end{cases},$$

with γ_l being a free parameter. This definition ensures $\|e^{\gamma_l}\| \approx 1$ on the actuator grid of each mirror. For the results presented subsequently we let $\gamma_1 = 1$, $\gamma_2 = 1.05$ and $\gamma_3 = 1.12$ in case of natural guide stars. For laser guide stars we chose $\gamma_1 = 0.95$, $\gamma_2 = 1$ and $\gamma_3 = 1.07$. Using this mollifier e^{γ_l} , the l -th mollifying vector is given by $\bar{e}_l^\gamma = (c_l e^{\gamma_l} \delta_{i,l})_{i=1,\dots,L}$.

The second step is to solve equation (23) via the iteration procedure (25) in order to obtain the reconstruction kernels. An example is given in Figure 5.1. In order to get an idea about the reconstruction quality, we can check the mollifier vector obtained from the reconstruction kernels. In the optimal case we would get $\mathcal{A}^* \psi_l^\gamma = \bar{e}_l^\gamma$ for $l = 1, 2, 3$. However, since we can only solve the normal equation, i.e., look for an approximate solution, we end up with some artefacts from layers that should be zero in the case of optimal reconstruction, see Figure 5.1. However, due to Lemma 4.4 it is not possible to avoid this as the information is encoded in the reconstruction kernels and cannot be removed artificially. In a last step we reconstruct the layers via $\Phi_\gamma^{(l)}(x) = \langle \varphi, T_{2,l}^x \Psi_l^\gamma \rangle_{(L_2(\mathbb{R}^2))^G}$ for each x corresponding to an actuator of the deformable mirror.

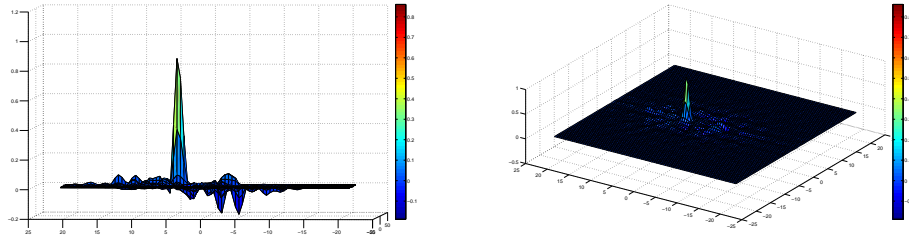


Figure 5: Reconstruction kernel Ψ_3^γ for layer 3 and a laser guide star

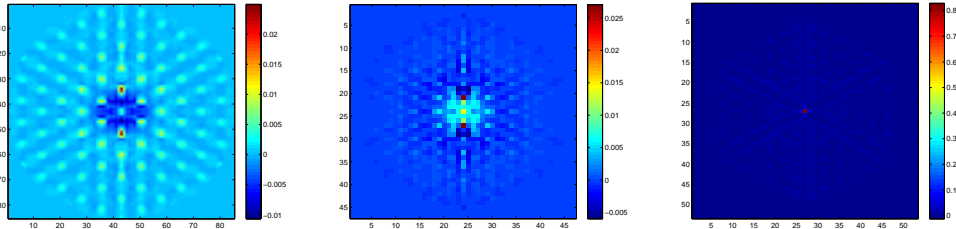


Figure 6: Mollification vector \bar{e}_l^γ obtained from reconstruction kernels for $\mathcal{A}^*\Psi_3^\gamma$ for the reconstruction of layer 3. From left to right: $(\mathcal{A}^*\Psi_3^\gamma)^{(l)}$ for $l = 1, 2, 3$. Although the third layer is reconstructed adequately, the other layers show some artefacts instead of being plain zero as would be the optimal case.

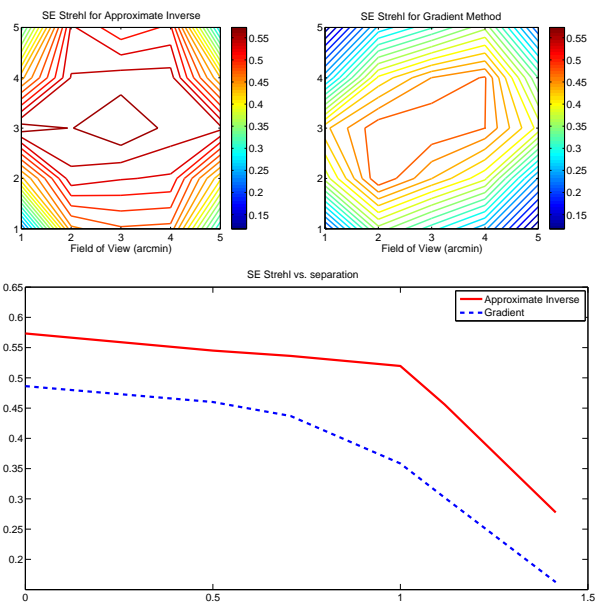
5.2 Simulation results

We compare the performance of the method of the approximate inverse (AI) with a gradient-based algorithm [40] that is known to produce solutions of the same quality as the methods currently used in practice for smaller telescopes. As evaluation criterion we use the short exposure (SE) Strehl ratio in K-band (for a wavelength of 2200 nm) after one time steps of 2 ms, according to the frequency of the AO system. The Strehl ratio, taking values in the interval $[0, 1]$, is a measure commonly used in Adaptive Optics for the observed image quality with higher values corresponding to better observed images. Running the simulation against the gradient method, we observe that the AI method performs better than the gradient method if the guide star types are not mixed, see Figure 7 and Figure 8. In these figures, the top image shows the Strehl over the whole field of view, whereas in the bottom picture we show the Strehl versus separation. Since the invariances of Theorem 4.3 only hold for a single type of guide stars used, we expect a slight drop in reconstruction quality when both guide star types are mixed. Numerical results confirm this, see Figure 9. We limit ourselves to one time step here since the design of a proper temporal control algorithm for the mirror updates is out of scope of this paper. Closing this gap remains future work.

5.3 Computational complexity

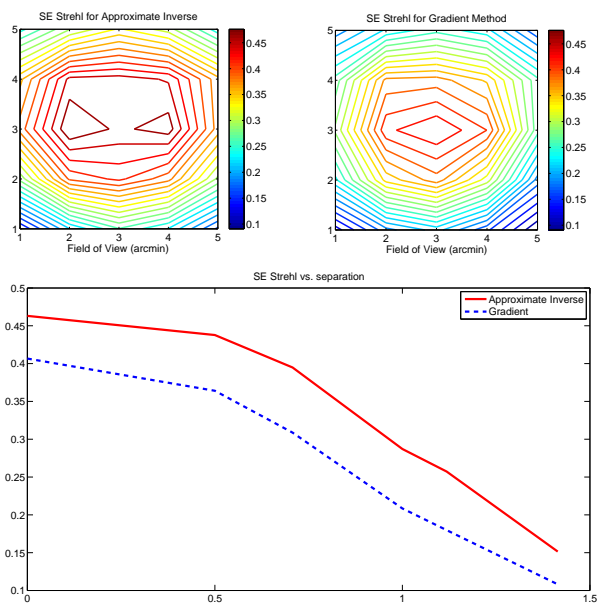
In adaptive optics, speed is one of the most critical criteria for acceptance of a method. For the approximate inverse, the situation is as follows. In a first step, the wavefronts have to be reconstructed for each guide star from the Shack-Hartmann wavefront sensors with CuReD. The computational complexity is $20n_{wfs}$ where n_{wfs} is the number of subapertures in the Shack-Hartmann wavefront sensor [21]. This has to be done for each of the G guide stars. CuReD is parallelizable.

The reconstructed wavefronts are then used to calculate the shape of the deformable mirrors using the reconstruction kernels. Since the kernels do not depend on the data, they can be precomputed. Hence this rather time consuming step gives no contribution during the actual computations. In particular, no runtime evaluation of the forward or adjoint operator is needed. The remaining effort lies in the evaluation of the scalar products. For the reconstruction of a single point of one layer, G inner products are required, each consisting of $2 \cdot n_{wfs}$ operations for the actual



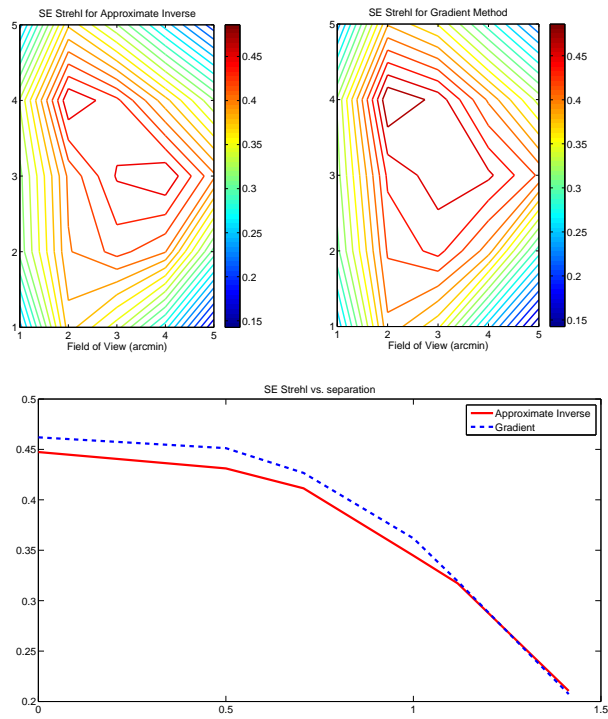
average Strehl: 0.469 (AI), 0.343 (Gradient)

Figure 7: Strehl for 6 natural guide stars



average Strehl: 0.334 (AI), 0.268 (Gradient)

Figure 8: Strehl for 6 laser guide stars



average Strehl: 0.342 (AI), 0.352 (Gradient)

Figure 9: Strehl for 6 laser guide stars and 3 natural guide stars

evaluation and, if the invariance operators from Theorem 4.3 are used, additional $6n_{wfs}$ operations to interpolate the reconstruction kernels on the grid of the deformable mirrors. Since we can reconstruct the artificial layers directly on the deformable mirrors, we have to do this for n_{act} points, where n_{act} denotes the combined number of actuators for all mirrors. Assuming that for each mirror we have approximately n_{wfs} actuators, the overall complexity for the reconstruction of a whole atmosphere in one time step is $G \cdot 20 \cdot n_{wfs} + n_{act} \cdot G \cdot 2n_{wfs} \cdot 6 \cdot n_{wfs} \approx G \cdot 20 \cdot n_{wfs} + 12L \cdot G \cdot n_{wfs}^3$. Using the alternative invariance operators from Remark 4.5, we can avoid the interpolation of the reconstruction kernels, but require an interpolation of the reconstructed mirror shape to its actual domain. However, since there are only very few layers compared to the huge amount of actuators, the computational cost is significantly reduced. The overall complexity can then be estimated as $G \cdot 20 \cdot n_{wfs} + n_{act} \cdot G \cdot 2n_{wfs} + 6 \cdot n_{act} \approx G \cdot 26 \cdot n_{wfs} + 12L \cdot G \cdot n_{wfs}^2$. Since each inner product is independent of the other ones, the procedure is highly parallelizable. Note that, due to the nature of the method, an extension of the model, e.g., an inclusion of additional effects of laser guide stars, does not increase the relevant computational effort as all operations involving the model are solely performed in the calculation of the reconstruction kernels.

Acknowledgements

D. Gerth and R. Ramlau were funded by the Austrian Science Fund (FWF): W1214–N15, project DK08. The cooperation of the authors was initiated by a visit of B. Hahn at Johannes Kepler University Linz, funded by the Doctoral Program “Computational Mathematics”, Johannes Kepler University Linz. D. Gerth would like to thank Daniela Saxenhuber (JKU Linz, Austria) for the fruitful discussions.

References

- [1] Auzinger G 2014 *New Reconstruction Approaches in Adaptive Optics for Extremely Large Telescopes*, PhD thesis, Johannes Kepler University Linz, 2014

- [2] Vogel C R and Yang Q 2006 Fast optimal wavefront reconstruction for multi-conjugate adaptive optics using the Fourier domain preconditioned conjugate gradient algorithm *Optics Express* **14**
- [3] Davison M A 1983 The ill-conditioned nature of the limited angle tomography problem *SIAM J. Appl. Math.* **43** 428–448
- [4] De Cezaro A and Haltmeier M and Leitão A and Scherzer O 2008 On Steepest-Descent-Kaczmarz methods for regularizing systems of nonlinear ill-posed equations *App. Math. Comput.* **202** 596–607
- [5] Ellerbroek B and Gilles L and Vogel C R 2002 A Computationally Efficient Wavefront Reconstructor for Simulation or Multi-Conjugate Adaptive Optics on Giant Telescopes *Proc. SPIE* **4839**
- [6] Ellerbroek B and Gilles L and Vogel C R 2003 Numerical simulations of multiconjugate adaptive optics wavefront reconstruction on giant telescopes *Applied Optics* **42**
- [7] Ellerbroek B and Vogel C R 2003 Simulations of closed-loop wavefront reconstruction for multiconjugate adaptive optics on giant telescopes *Proc. SPIE* **5169** 206–217
- [8] Louis A K 1996 Approximate inverse for linear and some nonlinear problems *Inverse Problems* **12** 175–190
- [9] Likht M K 1967 On the calculation of functionals in the solution of linear equations of the first kind *USSR Comput. Math. and Math. Phys.* **7** 271–8
- [10] Louis A K and Maass P 1990 A mollifier method for linear operator equations of the first kind *Inverse Problems* **6** 427–440
- [11] Louis A K 2011 Feature reconstruction in inverse problems *Inverse Problems* **27** 065010(21pp)
- [12] Schuster T and Schöpfer F 2010 Solving linear operator equations in Banach spaces non-iteratively by the method of approximate inverse *Inverse Problems* **26** 085006(19pp)
- [13] Schuster T 2007 *The method of approximate inverse: theory and applications (Lecture Notes in Mathematics Vol. 1906)* Springer, Berlin

- [14] Schuster T 2001 An efficient mollifier method for three-dimensional vector tomography: convergence analysis and implementation *Inverse Problems* **17** 739–766
- [15] Ellerbroek B L and Vogel C R 2009 Inverse problems in astronomical adaptive optics *Inverse Problems* **25** 1–37
- [16] Ellerbroek B L 2002 Efficient computation of minimum-variance wavefront reconstructors with sparse matrix techniques *J. Opt. Soc. Am.* **19** 1803–1816
- [17] Gilles L and Vogel C R and Ellerbroek B L 2002 Multigrid preconditioned conjugate-gradient method for large-scale wave-front reconstruction *J. Opt. Soc. Am. A* **19** 1817–1822
- [18] Thiébaud E and Tallon M 2010 Fast minimum variance wavefront reconstruction for extremely large telescopes *J. Opt. Soc. Am. A* **27** 1046-1059
- [19] Zhariy M and Neubauer A and Rosensteiner M and Ramlau R 2011 Cumulative Wavefront Reconstructor for the Shack-Hartman Sensor *Inverse Problems and Imaging* **5** 893–913
- [20] Rosensteiner M 2011 Cumulative Reconstructor: fast wavefront reconstruction algorithm for Extremely Large Telescopes *J. Opt. Soc. Am. A* **28** 2132–2138
- [21] Rosensteiner M 2012 Wavefront reconstruction for extremely large telescopes via CuRe with domain decomposition *J. Opt. Soc. Am. A* **29** 2328–2336
- [22] Rigaut F J and Ellerbroek B L and Flicker R 2000 Principles, limitations and performance of multiconjugate adaptive optics *Proc. SPIE* **4007** 1022–1031
- [23] Gavel D 2004 Tomography for multiconjugate adaptive optics systems using laser guide stars *SPIE Astronomical Telescopes and Instrumentation* **5490** 1356–1373
- [24] Fusco T and Conan J-M and Rousset G and Mugnier L M and Michau V 2001 Optimal wave-front reconstruction strategies for multi conjugate adaptive optics *J. Opt. Soc. Am. A* **18** 2527–2538

- [25] Ramlau R and Rosensteiner M 2012 An efficient solution to the atmospheric turbulence tomography problem using Kaczmarz iteration *Inverse Problems* **28** 095004
- [26] Marchetti E and Brast R and Delabre B et al 2007 On-sky Testing of the Multi-Conjugate Adaptive Optics Demonstrator *The Messenger* **189** 8–13
- [27] Gilles L and Ellerbroek B and Vogel C R 2002 Layer-Oriented Multi-grid Wavefront Reconstruction Algorithms for Multi-Conjugate Adaptive Optics *Proc. SPIE* **4839**
- [28] Gilles L and Ellerbroek B and Vogel C R 2003 Preconditioned conjugate gradient wave-front reconstructors for multiconjugate adaptive optics *Applied Optics* **42** 5233–5250
- [29] Gilles L and B. Ellerbroek and Vogel C R 2007 A comparison of Multi-grid V-cycle versus Fourier Domain Preconditioning for Laser Guide Star Atmospheric Tomography *in: Adaptive Optics: Analysis and Methods/Computational Optical Sensing and Imaging/Information Photonics/Signal Recovery and Synthesis Topical Meetings on CD-ROM, OSA Technical Digest (CD)* Optical Society of America
- [30] Gilles L and Ellerbroek B 2008 Split atmospheric tomography using laser and natural guide stars *J. Opt. Soc. Am.* **25** 2427–35
- [31] Yang Q and Vogel C R and Ellerbroek B 2006 Fourier domain preconditioned conjugate gradient algorithm for atmospheric tomography *Applied Optics* **45** 5281–5293
- [32] Tokovinin A and Le Louarn M 2000 Isoplanatism in a multiconjugate adaptive optics system *J. Opt. Soc. Am. A* **17** 1819–1827
- [33] Tokovinin A and Viard E 2001 Limiting precision of tomographic phase estimation *J. Opt. Soc. Am. A* **18** 873–882
- [34] Tallon M and Tallon-Bosc I and Béchet C and Momey F and Fradin M and Thiébaud E 2010 Fractal iterative method for fast atmospheric tomography on extremely large telescopes *Proc. SPIE* **7736**

- [35] Helin T and Yudytskiy M 2013 Wavelet methods in multi-conjugate adaptive optics *Inverse Problems* **29** 085003
- [36] Yudytskiy M and Helin T and Ramlau R 2013 A frequency dependent preconditioned wavelet method for atmospheric tomography *in: Third AO4ELT Conference - Adaptive Optics for Extremely Large Telescopes*
- [37] Ramlau R and Obereder A and Rosensteiner M and Saxenhuber D 2013 Efficient iterative tip/tilt reconstruction for atmospheric tomography *submitted*
- [38] Rosensteiner M and Ramlau R 2012 Efficient iterative atmospheric tomography reconstruction from LGS and additional tip/tilt measurements *in: SPIE 8447, Adaptive Optics Systems III* 84475S-84475S-6
- [39] Rosensteiner M and Ramlau R 2013 The Kaczmarz algorithm for multi-conjugate adaptive optics with laser guide stars *J. Opt. Soc. Am. A* **30** 1680–1686
- [40] Saxenhuber D and Ramlau R 2013 A Gradient-Based Method for Atmospheric Tomography *Austrian In-Kind Contribution - AO E-TRE-AAO-528-0043*

Technical Reports of the Doctoral Program

“Computational Mathematics”

2014

- 2014-01** E. Pilgerstorfer, B. Jüttler: *Bounding the Influence of Domain Parameterization and Knot Spacing on Numerical Stability in Isogeometric Analysis* February 2014. Eds.: B. Jüttler, P. Paule
- 2014-02** T. Takacs, B. Jüttler, O. Scherzer: *Derivatives of Isogeometric Functions on Rational Patches* February 2014. Eds.: B. Jüttler, P. Paule
- 2014-03** M.T. Khan: *On the Soundness of the Translation of MiniMaple to Why3ML* February 2014. Eds.: W. Schreiner, F. Winkler
- 2014-04** G. Kiss, C. Giannelli, U. Zore, B. Jüttler, D. Großmann, J. Barne: *Adaptive CAD model (re-)construction with THB-splines* March 2014. Eds.: M. Kauers, J. Schicho
- 2014-05** R. Bleyer, R. Ramlau: *An Efficient Algorithm for Solving the dbl-RTLS Problem* March 2014. Eds.: E. Klann, V. Pillwein
- 2014-06** D. Gerth, E. Klann, R. Ramlau, L. Reichel: *On Fractional Tikhonov Regularization* April 2014. Eds.: W. Zulehner, U. Langer
- 2014-07** G. Grasegger, F. Winkler, A. Lastra, J. Rafael Sendra: *A Solution Method for Autonomous First-Order Algebraic Partial Differential Equations* May 2014. Eds.: P. Paule, J. Schicho
- 2014-08** W. Krendl, W. Zulehner: *A Decomposition Result for Biharmonic Problems and the Hellan-Herrmann-Johnson Method* August 2014. Eds.: U. Langer, V. Pillwein
- 2014-09** U. Langer, S. Repin, M. Wolfmayr: *Functional a Posteriori Error Estimates for Parabolic Time-Periodic Boundary Value Problems* August 2014. Eds.: V. Pillwein, W. Zulehner
- 2014-10** A. Maletzky: *Complexity Analysis of the Bivariate Buchberger Algorithm in Theorema* October 2014. Eds.: B. Buchberger, W. Schreiner
- 2014-11** C. Fürst, G. Landsmann: *The Concept of Gröbner Reduction for Dimension in Filtered Free Modules* October 2014. Eds.: F. Winkler, J. Schicho
- 2014-12** D. Gerth, B.N. Hahn, R. Ramlau: *The Method of the Approximate Inverse for Atmospheric Tomography* December 2014. Eds.: U. Langer, W. Zulehner

Doctoral Program

“Computational Mathematics”

Director:

Prof. Dr. Peter Paule
Research Institute for Symbolic Computation

Deputy Director:

Prof. Dr. Bert Jüttler
Institute of Applied Geometry

Address:

Johannes Kepler University Linz
Doctoral Program “Computational Mathematics”
Altenbergerstr. 69
A-4040 Linz
Austria
Tel.: ++43 732-2468-6840

E-Mail:

office@dk-compmath.jku.at

Homepage:

<http://www.dk-compmath.jku.at>